Actinic Inspection of EUV Programmed Multilayer Defects and Cross-Comparison Measurements

Kenneth A. Goldberg[1], Anton Barty[2], Yanwei Liu[1], Patrick Kearney[3], Yoshihiro Tezuka[4], Tsuneo Terasawa[4], John S. Taylor[2], Hak-Seung Han[3] and Obert R. Wood II[3]
[1]*Lawrence Berkeley National Laboratory, Berkeley, CA 94720, USA*
[2] *Lawrence Livermore National Laboratory, Livermore, CA 94550, USA*
[3]*SEMATECH, 255 Fuller Road, Suite 309, Albany, NY 12203, USA*
[4]*MIRAI – Association of Super-Advanced Electronics Technologies, 16-1 Onogawa, Tsukuba, Ibaraki 305-8569, Japan*

The production of defect-free mask blanks remains a key challenge for extreme ultraviolet (EUV) lithography. Integral to this effort is the development and characterization of mask inspection tools that are sensitive enough to detect critical defects with high confidence. Using a single programmed-defect mask with a range of buried bump-type defects, we report a comparison of measurements made in four different mask-inspection tools: one commercial tool using 488-nm wavelength illumination, one prototype tool that uses 266-nm illumination, and two non-commercial EUV "actinic" inspection tools. The EUV tools include a darkfield imaging microscope and a scanning microscope. Our measurements show improving sensitivity with the shorter wavelength non-EUV tool, down to 33-nm spherical-equivalent-volume diameter, for defects of this type. Measurements conditions were unique to each tool, with the EUV tools operating at a much slower inspection rate. Several defects observed with EUV inspection were below the detection threshold of the non-EUV tools.

I. INTRODUCTION

Operating near 13-nm wavelength, EUV projection lithography is reliant on nearly perfect reflective surfaces. Multilayer coatings applied across atomically smooth substrates give EUV mirrors reflectivities as high as approximately 70%. The imaging lenses used in EUV lithography are arguably the highest quality optical imaging systems ever produced; they are

[1] email address: KAGoldberg@lbl.gov

typically comprised of 2 to 6 aspheric elements with surface figure and finish tolerances in the sub-nanometer range. Equally important are the patterned reticles fabricated with absorbing and/or phase-shifting features on thick mirror substrates.

Any disruption in the electric field reflected from the reticle has the potential to print on the wafer and cause device failure. Therefore the inspection of EUV reticles before and after patterning is critical to the success of EUV lithography. Given the increasing cost of a production mask set, accurate and reliable inspection potentially offers significant economic advantages in terms of mask cost. Speed and accuracy of inspection with sensitivity to the smallest printable defects is of primary concern, with mask blank inspection before patterning offering great potential to save mask makers a from wasting time and effort on an imperfect substrate.

Separate from large-scale variations in the coating thickness, which cause a shift in the spectral response of the multilayer, small-scale defects are a particular concern. Many types of critical defects have been identified, including both *absorptive defects* [1, 2] and *phase defects* [3, 4]. EUV light is particularly susceptible to the presence of light-absorbing particles or thin layers of material on mirror surfaces; such defects can introduce phase shifts and significant local attenuation. Separately, *substrate defects*, bumps or pits, which are buried beneath the multilayer, can create local changes in the top surface profile. The reflectivity changes depend strongly on the multilayer deposition conditions [5, 6], but often these substrate defects will primarily affect the phase of the reflected light through path length differences or multilayer thickness effects, leaving the amplitude relatively constant [4]. For any defect type, reflection from the reticle typically enhances the deleterious effects by doubling the interaction path length, or path length difference.

Owing to the resonant-reflective properties of the multilayer coating, the nature and observability of reticle defects are highly wavelength-dependent [7, 8]. In particular, what constitutes a π-phase defect for EUV light may make insignificant changes at other wavelengths. Since most commercial mask blank inspection tools do not use EUV light, understanding the efficacy of these tools requires cross-comparison testing against EUV measurements and/or

lithographic printing results, although currently, the utility of printing results for such a comparison can be limited by the resolution of experimental modern photoresist materials [9]. The comparison presented here represents the current state of the art, made with the best available data for a single programmed-defect mask. Results for other programmed-defect types and for native defects occurring with different multilayer deposition methods will be the subjects of future research.

II. EXPERIMENT DESCRIPTION

A single programmed-defect mask was measured in four different mask inspection tools; the results are compared in this report. The mask was developed by Hoya and supplied by MIRAI (serial no. MIRAI DEF03B), and some inspection results from this mask have been reported previously [10, 11]. In addition to fiducial marks, it contains a 150 × 500-μm wide array of buried substrate defects created from 7-nm-thick CrN pads patterned below the multilayer coating. Defects of different sizes are arranged in nine columns with 49 similar defects per column. When measured with atomic force microscopy (AFM) after multilayer coating, the top surface shows two types of profiles: truncated (flat topped) pyramids (*TP type*) and Gaussian bumps (*G type*). The surface profiles range from 420-nm wide × 7-nm high, TP-type, to as small as 70-nm wide × 3.5-nm high, G-type for the smallest defects. A ninth column suffered from resist collapse leading to irregular sizes, and an intended tenth column did not print. In addition there is a rectangular border constructed of large defects surrounding the programmed-defect array.

A. The MIRAI darkfield imaging tool. This mask was first measured with EUV light by Tezuka using an EUV darkfield imaging microscope developed by MIRAI [10, 11]. In this system, a tantalum target is irradiated by a YAG laser producing EUV light, which is filtered by a Zr filter followed by an ellipsoidal mirror. Close to the mask, a small plane folding mirror directs the converging light toward the mask at normal incidence. Scattered, *darkfield* light reflected from the reticle is collected by a 20× magnification Schwarzschild objective with an

annular pupil subtending 0.1 to 0.2 numerical aperture (NA), aligned at normal incidence to the mask. The objective projects the darkfield image onto a low-noise scientific grade charge-coupled device (CCD) where an entire image field is recorded at once. Careful calibrations are performed to normalize the recorded signal [11]. The MIRAI tool was able to detect all of the programmed defects with a high signal-to-noise ratio (SNR) and also noted the presence of a few "native" defects that appeared after the measurements presented here.

B. The Berkeley actinic inspection tool. The Berkeley actinic inspection system [12], operated by Goldberg, Barty and Liu, illuminates the mask with EUV light yet records data in a much different manner than the MIRAI tool. A bending magnet beamline at LBNL's Advanced Light Source provides monochromatic illumination to a pinhole; a 20×-demagnification Schwarzschild objective re-images the illuminated pinhole onto the upward-facing reticle with a 6° angle of incidence. During measurement, the beam focus remains stationary while the mask is translated and rotated (r, θ) in a manner that allows a portion of the mask to be scanned. Using different pinhole diameters, the beam size on the reticle can be varied from 1 μm to 5 μm: these measurements were made with a 2.5-μm diameter beam.

The Berkeley inspection system is flexible in its detector geometry, and is capable of simultaneously recording brightfield and darkfield signals at up to 100kHz. The inspection data presented here was recorded with a new detector design that records darkfield light in an off-axis angular range of 0.6°–35° from the central ray in one direction, and ±4.3° in the perpendicular direction, and with no intervening mirrors between the mask and the detector. In this way the darkfield detection comes close to the specular beam; the detector was positioned to provide optimal SNR for the defects in this study.

C. Two Lasertec inspection tools. The test mask was also measured in two non-EUV inspection tools, both created by Lasertec Corp., and operated for these measurements by Kearney.

The Lasertec M1350, introduced in 2002, uses an argon-ion laser to generate light at the 488-nm illumination wavelength. The scanning confocal system uses a Multiple Image Acquisition for Giga-bit Inspection with Confocal System (MAGICS) configuration to achieve

both high throughput and sensitivity. On transparent mask substrates, the M1350 can scan the entire 200-cm^2 quality area in 20 minutes; it has previously demonstrated polystyrene latex (PSL)-equivalent-size sensitivity below 60 nm [7, 8].

The mask was also measured in a new Lasertec inspection tool still under development at Lasertec. The Lasertec MB266 uses 266-nm wavelength ultra-violet light and operates in a similar manner to the M1350.

III. RESULTS

The comparison presented here represents the best available data from each tool as of June 2006. The methods and details of each individual measurement are quite different. The tools were designed to meet different performance metrics, and the data should be considered within the context of those differences. In particular, the Lasertec tools are designed for high throughput, large-area scanning. In contrast, the EUV tools are designed for research and were created to provide reference measurements for cross-comparisons such as this. While each of the tools may be able to improve sensitivity by increasing the measurement time, this is especially true for the Lasertec tools, which scan mask areas from 40 to several thousand times faster than the EUV tools, depending on measurement conditions. We also note that the Lasertec MB266 had not yet been released at the time of measurement; as such, its sensitivity may continue to improve over time. For this reason, at Lasertec's request, only qualitative measurement results from this tool are presented.

For the two actinic tool measurements, the analysis presented here was performed on the raw inspection data. The defect strengths are compared with the background signal to determine the SNR of each measured defect in the array. The Lasertec tools report defect positions and sizes based on "pixels." The detection threshold for the Lasertec tools is set high (approximately 7 σ) to avoid false positives within the measurement of the entire quality area of a mask under inspection.

A. Actinic inspection data. SNR calculations made from the inspection results of the two EUV tools are shown in Figs. 1 and 2. The MIRAI data is collected in the form of a single darkfield image of the field. For the MIRAI tool, the SNR calculation is based on examining the integrated signal strength within an area of approximately 11 μm^2 centered at each known defect position. A careful normalization and background subtraction are performed using a local average over measured points between the defect positions. The noise level is calculated from an ensemble of 98 patches collected from defect-free regions of the image, treated in an identical manner as the defect regions.

The Berkeley data is acquired from a scanning measurement. Data was collected during a slow speed scan, with a 5-μm beam diameter on the mask and adjacent scan lines separated by 1 μm. For this measurement, the amplifier bandwidth limits independent measurements to approximately 0.1-μm separation in the scan direction. Following normalization to the background signal level, the raw data is used to reconstruct a two-dimensional *image* of the programmed defect region with 1-μm pixel grid. Once this image is calculated, the SNR calculation follows the same method applied to the MIRAI data, with local background subtraction, and the noise level calculated from 98 defect-free patches in adjacent areas of the same data set. A brightfield scan of the region revealed the presence of a few native defects that appeared on the mask following the collection of the MIRAI data shown here. The calculation of the Berkeley tool's column-averaged SNR values excludes the programmed defects covered by these native defects.

Relative to the measured noise level in small areas within defect-free areas, σ, a detection threshold value of 3.25 σ was set for the EUV measurements, based on a 50% probability of a single false-positive within the programmed-defect region of interest.

B. Lasertec-tool inspection data. The Lasertec data, shown in Fig. 3, represents the *pixel* size of each defect found in the programmed-defect region. Column averages for the pixel size of detected defects and the capture efficiency (CE) of the Lasertec M1350 are shown in Fig 4. On this mask, the M1350 was able to detect 100% of defects down to 47-nm PSL-equivalent-volume

diameter. The MB266 detected significantly more of the defects in the columns with the two smallest sizes.

IV. CONCLUSION

The interaction of reflected EUV light with defects on or below a mask surface is a complex process that is highly wavelength-dependent. However, the necessity of EUV "actinic" inspection for the commercial production of defect-free EUV mask blanks remains an open question whose answer depends on sensitivity improvements in non-EUV inspection tools. The resonant reflective properties of EUV multilayer coatings make cross-comparison between EUV and non-EUV inspection tools critically important to the evaluation of new tools now under development and future tools as well. EUV inspection in both brightfield and darkfield modes provides quantitative feedback with high spatial resolution in a manner that is beyond the capabilities of traditional reflectometers or printing tests. For evaluating surface defects, bump and pit-type substrate defects, and novel defect-repair strategies, the cross-comparison with EUV inspection will provide vital feedback and risk reduction.

We have inspected a bump-type buried substrate defect mask in four different state of the art inspection tools: two EUV research tools and two non-EUV tools produced by Lasertec. The EUV MIRAI darkfield imaging tool was able to easily detect every defect on the mask with high SNR. The Berkeley tool detected most of the defects, down to the smallest sizes, with lower SNR than the MIRAI tool. The Berkeley tool also provides brightfield reflectivity information, which clearly detects native surface defects. The Lasertec M1350, which operates at 488-nm wavelength, was able to detect 100% of the defects down to a 47-nm PSL-equivalent-volume diameter, but had a lower capture efficiency below that level. The fourth tool was a pre-release Lasertec MB266, which operates at 266-nm wavelength and is significantly more sensitive to defects of this type than the M1350. The MB266 detected a majority of the defects at 33 nm and 41 nm, and, like the M1350, it detected 100% of the defects larger than those sizes. We note that

the MB266 sensitivity may improve as the tool is optimized, and that this data is based on a pre-release tool.

Additional comparisons involving defects of different sizes, shapes, and multilayer deposition methods will continue to provide quantitative data for tool evaluation and strategic decision-making regarding the commercial need for actinic inspection of EUV masks. Of particular interest will be the future inspection of defect-repair strategies that may rely on the resonant-reflective multilayer properties to minimize disturbances of the EUV beam, but may appear as defects in inspections performed at other wavelengths.

V. ACKNOWLEDGMENTS

The authors gratefully acknowledge funding support from SEMATECH under contract LITH-343, and NEDO. We are also grateful to Hoya for providing the mask, and Lasertec for their support of this work. CXRO scientific and technical staff members who have been instrumental in this work include: Senajith Rekawa, C. Drew Kemp, and Eric Gullikson, and others. Parts of this were performed under the auspices of the U.S. Department of Energy by the University of California, Lawrence Livermore National Laboratory under contract No. W-7405-Eng-48 and Lawrence Berkeley National Laboratory under contract No. DE-AC02-05CH11231.

REFERENCES

1. T. Liang, A. Stivers. R. Livengood, P.-Y. Yan, G. Zhang, and F.-C. Lo, *Journal of Vacuum Science and Technology B* **18** (6), 3216 (2000).
2. M. Yi, S. Jeong, S. Rekawa, and J. Bokor, *Journal of Vacuum Science and Technology B* **18** (6), 2930 (2000).
3. E.M. Gullikson, C. Cerjan, D.G. Stearns, P.B. Mirkarimi, and D.W. Sweeney, *Journal of Vacuum Science and Technology B* **20** (6), 81 (2002).
4. E. M. Gullikson, E. Tejnil, T. Liang, A. R. Stivers, *Proc. SPIE* **5374**, 791 (2004).

5. P. B. Mirkarimi and D. G. Stearns, *Appl. Phys. Lett.* **77**, 2243 (2000).
6. D.G. Stearns, P. B. Mirkarimi, E. Spiller, *Thin Solid Films* **446** 37 (2004).
7. E. M. Gullikson, E. Tejnil, K.-Y. Tsai, A. R. Stivers, H. Kusunose, *Proc. SPIE* **5751**, 1223 (2005).
8. K.-Y. Tsai, E. Gullikson, P. Kearney, A. Stivers, *Proc. SPIE* **5992**, 1178 (2005).
9. P. Naulleau, C. Rammeloo, J. Cain, K. Dean, P. Denham, K. Goldberg, B. Hoef, B. La Fontaine, A. Pawloski, C. Larson, and G. Wallraff, *Proc. SPIE* **6151**, *to be published* (2006).
10. Y. Tezuka, M. Ito, T. Terasawa and T. Tomie, *Proc. SPIE* **5374**, 271 (2004).
11. Y. Tezuka, M. Ito, T. Terasawa and T. Tomie, *Proc. SPIE* **5567**, 791 (2004).
12. Y. Liu, A. Barty, E. Gullikson, J. S. Taylor, J. A. Liddle and O. Wood, *Proc. SPIE* **5751**, 660 (2005).

FIGURE CAPTIONS

Fig. 1. EUV "actinic" inspections of the programmed defect region. (**Left)** MIRAI tool data, **(right)** Berkeley tool darkfield data. Square area corresponds to the measured SRN—figures are individually scaled for each tool. Open squares represent defects below 3.25 σ detection threshold. Gray diamonds represent the relative size and location of surface contamination that occurred at some point after the MIRAI inspection shown here. Those dark regions were observed in the brightfield response measured with the Berkeley tool.

Fig. 2. Column averages of the measured SNR in the two EUV tools. For each column, the AFM-measured surface width and height of the defects is given, along with the PSL-equivalent-volume diameter (d_{SEV}). The defect surface shape is indicated with *G* for Gaussian and *TP* for truncated pyramid.

Fig. 3. Lasertec inspections of the programmed defect region: **(left)** M1350 (λ = 488 nm), and **(right)** MB266 (λ = 266 nm). The square areas correspond to the "pixel" size of the above-threshold defects. The positions of several native defects are shown as gray diamonds: their pixel size was reported as 2–10× higher than the largest programmed defects.

Fig. 4. Column averages of the measured pixel size **(dashed line)** for the defects above detection threshold as detected by the M1350. The capture efficiency (CE) is shown (**solid line)** for each defect size.

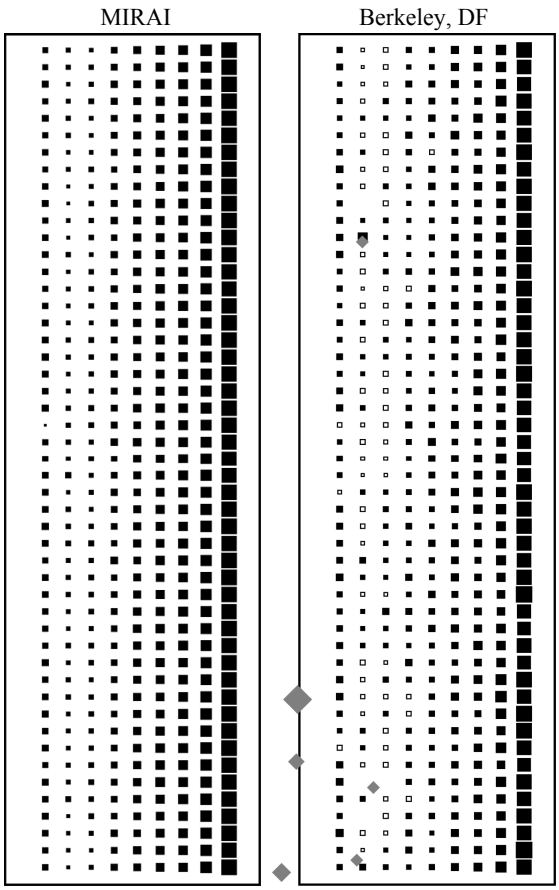

(sized for a 3" column width)

Fig. 1. EUV 'actinic' inspections of the programmed-defect region. (**Left)** MIRAI tool data, **(right)** Berkeley tool darkfield data. Square area corresponds to the measured SRN—figures are individually scaled for each tool. Open squares represent defects below 3.25 σ detection threshold. Gray diamonds represent the relative size and location of surface contamination which occurred at some point after the MIRAI inspection shown here. Those dark regions were observed in the bright-field response measured with the Berkeley tool.

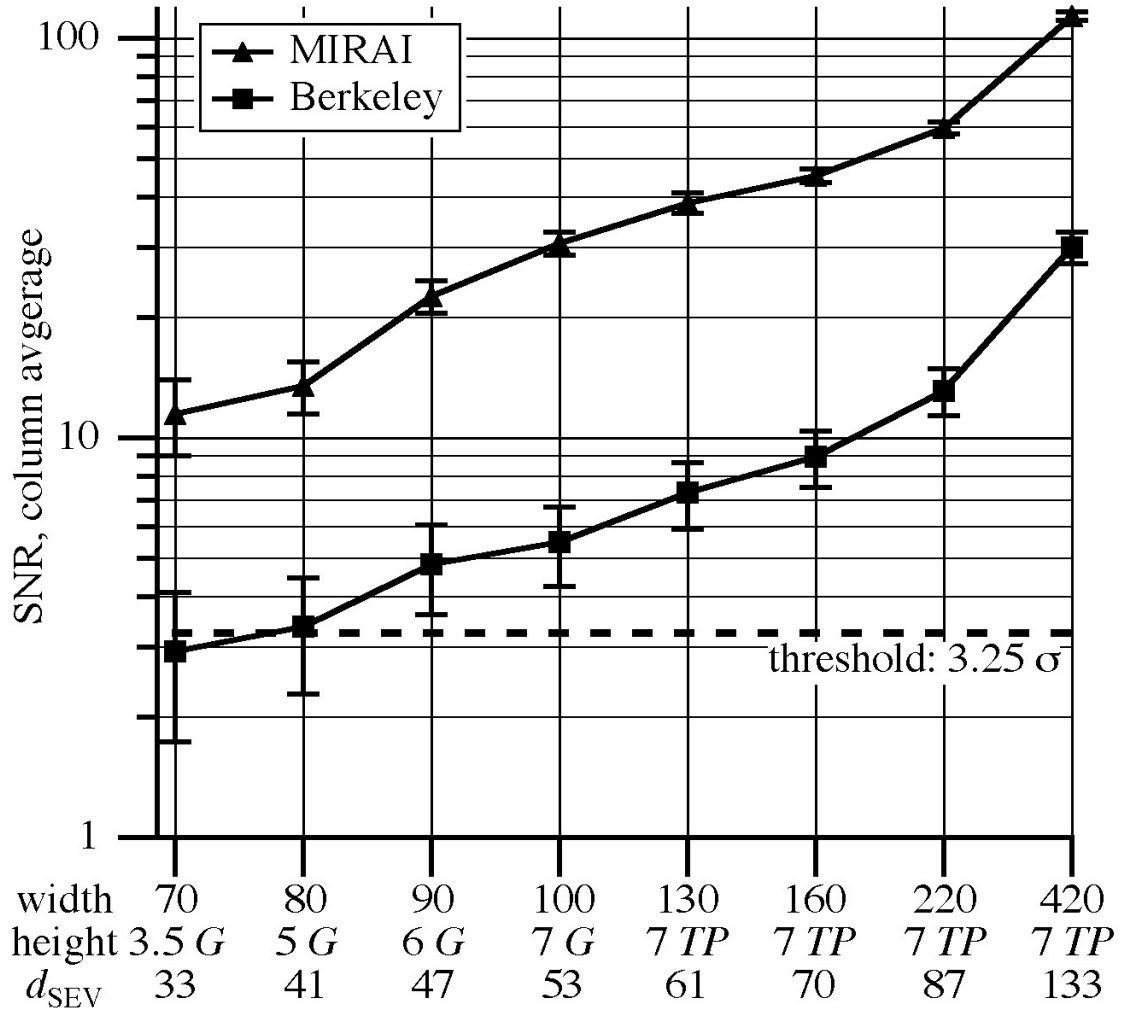

(sized to be reduced 50%)

Fig. 2. Column-averages of the measured SNR in the two EUV tools. For each column, the AFM-measured surface width and height of the defects is given, along with the spherical-equivalent-volume diameter (d_{SEV}). The defect surface shape is indicated with *G* for Gaussian, and *TP* for truncated pyramid.

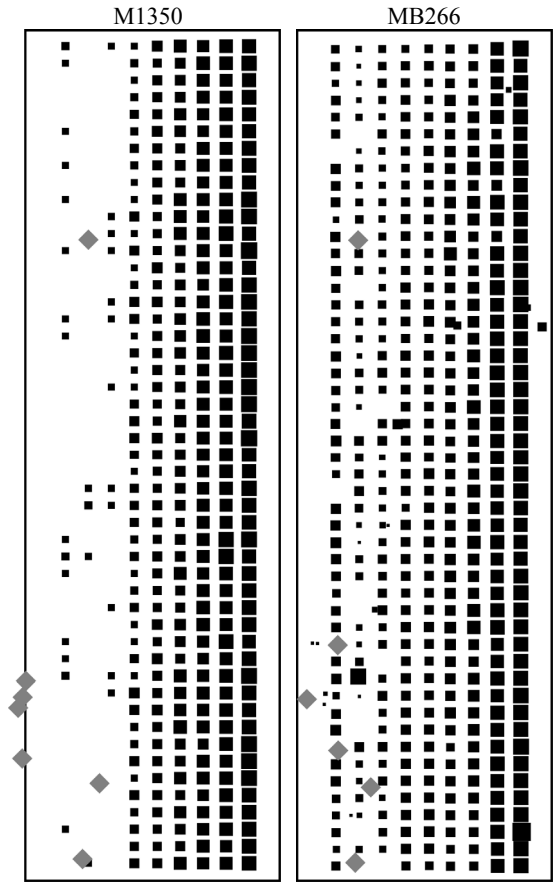

(sized for a 3" column width)

Fig. 3. Lasertec inspections of the programmed defect region: **(left)** M1350 (λ = 488-nm), and **(right)** MB266 (λ = 266-nm). The square areas correspond to the 'pixel' size of the above-threshold defects. The positions of several native defects are shown as gray diamonds: their pixel size was reported as 2–10 times higher than the largest programmed defects.

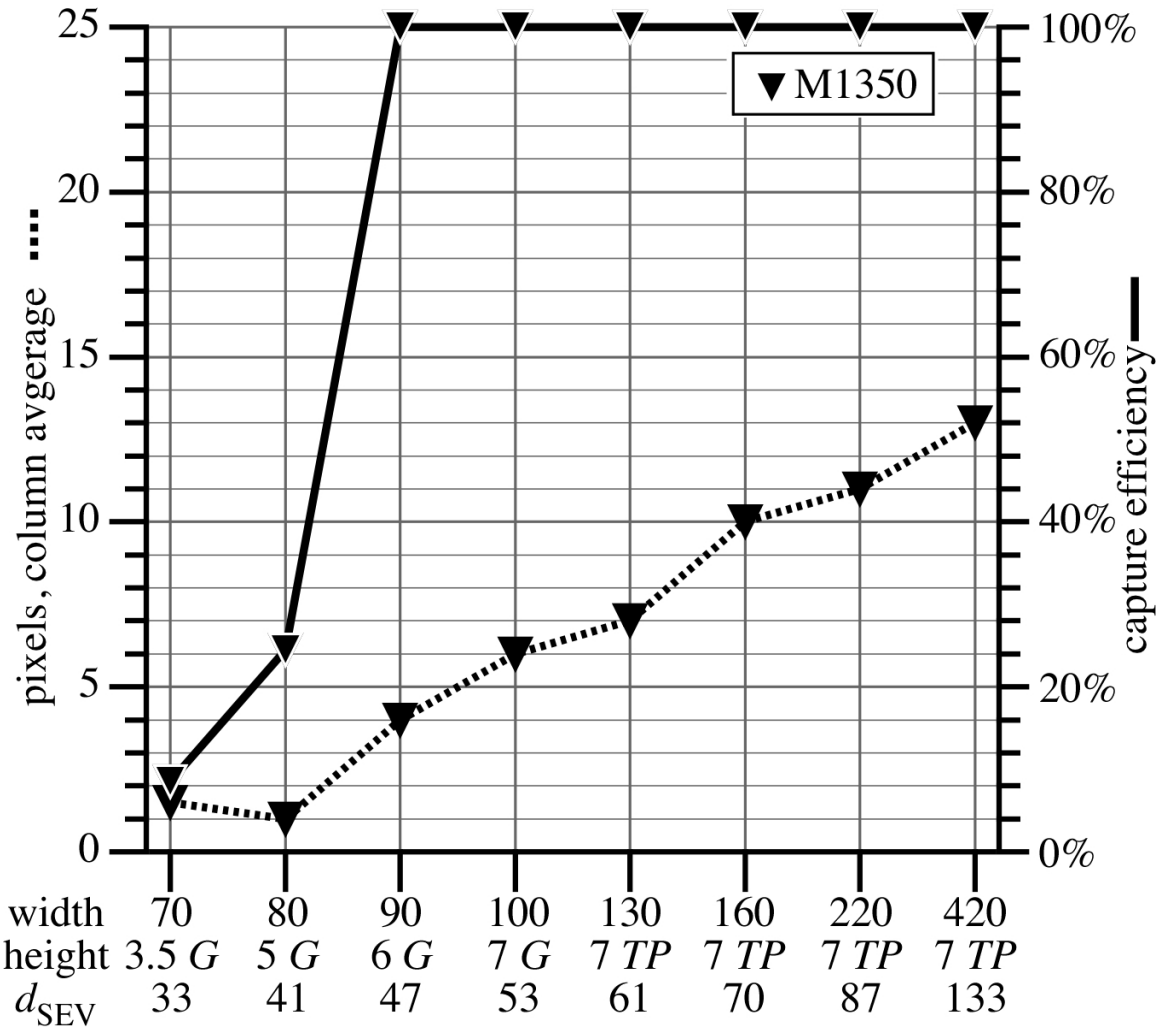

(sized to be reduced 50%)

Fig. 4. Column-averages of the measured pixel size **(dashed line)** for the defects above detection threshold as detected by the M1350. The capture efficiency (CE) is shown (**solid line)** for each defect size.